Journal of Neuroimaging

WILEY

JOURNAL OF NEUROIMAGING
THE OFFICIAL JOURNAL OF THE AMERICAN SOCIETY OF NEUROIMAGING

TECHNOLOGY UPDATES OPEN ACCESS

Assessing a Stimulator Modification for Simultaneous Noninvasive Auricular Vagus Nerve Stimulation and MRI

Vanessa Teckentrup[1,2] | Mareike Ludwig[3,4,5] | Janis Seibt[6,7] | Renée Hartig[8,9,10] | Hubert Preissl[11,12,13,14,15] | Mark Schuppert[16] | Nikolai I. Avdievich[16] | Klaus Scheffler[16,17] | Nikos Priovoulos[18,19,20] | Maik Ehses[21] | Benedikt A. Poser[22] | Christopher J. Wiggins[23] | Peter Trautner[24] | Walter Honerbach[25] | Heidi I. L. Jacobs[26,27] | Oliver Speck[6,28,29,30] | Dorothea Hämmerer[3,5,31,32,33] | Nils B. Kroemer[1,12,34]

[1]Department of Psychiatry and Psychotherapy, University of Tübingen, Tübingen, Germany | [2]School of Psychology, Trinity College Dublin, Dublin, Ireland | [3]Institute of Cognitive Neurology and Dementia Research, Otto-von-Guericke University Magdeburg, Magdeburg, Germany | [4]Department of Neurology, University Medical Center Hamburg-Eppendorf, Hamburg, Germany | [5]German Center for Neurodegenerative Diseases (DZNE), Magdeburg, Germany | [6]Department of Biomedical Magnetic Resonance, Otto-von-Guericke University Magdeburg, Magdeburg, Germany | [7]Research Campus STIMULATE, Otto Von Guericke University Magdeburg, Magdeburg, Germany | [8]Max Planck Institute for Biological Cybernetics, Tübingen, Germany | [9]Nathan S. Kline Institute for Psychiatric Research, Orangeburg, New York, USA | [10]Department of Psychiatry, Grossman School of Medicine, New York University, New York, New York, USA | [11]German Center for Diabetes Research (DZD), Tübingen, Germany | [12]German Center for Mental Health (DZPG), Partner Site Tübingen, Tübingen, Germany | [13]Division of Endocrinology, Diabetology and Nephrology, Department of Internal Medicine IV, University Hospital of Eberhard-Karls-University Tübingen, Tübingen, Germany | [14]Institute of Pharmaceutical Sciences, Department of Pharmacy and Biochemistry, Eberhard Karls University Tübingen, Tübingen, Germany | [15]Interfaculty Centre for Pharmacogenomics and Pharma Research at the Eberhard Karls University Tübingen, Tübingen, Germany | [16]Magnetic Resonance Center, Max Planck Institute for Biological Cybernetics, Tübingen, Germany | [17]Department of Biomedical Magnetic Resonance, University of Tübingen, Tübingen, Germany | [18]Spinoza Center for Neuroimaging, Amsterdam, The Netherlands | [19]Biomedical Engineering and Physics, Amsterdam UMC, Amsterdam, The Netherlands | [20]Wellcome Centre for Integrative Neuroimaging, FMRIB, Nuffield Department of Clinical Neurosciences, University of Oxford, Oxford, UK | [21]Department of Radio Frequency and Communication Technology, Otto-von-Guericke University Magdeburg, Magdeburg, Germany | [22]Faculty of Psychology and Neuroscience, Maastricht University, Maastricht, The Netherlands | [23]Imaging Core Facility (INM-ICF), Institut für Neurowissenschaften Und Medizin, Forschungszentrum Jülich, Jülich, Germany | [24]Core Facility Human 3T MRI, Faculty of Medicine, University of Bonn, Bonn, Germany | [25]Research and Technology Center for Detector Physics, University of Bonn, Bonn, Germany | [26]Gordon Center for Medical Imaging, Department of Radiology, Massachusetts General Hospital, Harvard Medical School, Boston, Massachusetts, USA | [27]Faculty of Health, Medicine and Life Sciences, School for Mental Health and Neuroscience, Alzheimer Centre Limburg, Maastricht University, Maastricht, The Netherlands | [28]Center for Intervention and Research on Adaptive and Maladaptive Brain Circuits Underlying Mental Health (C-I-R-C), Halle-Jena-Magdeburg, Magdeburg, Germany | [29]German Center for Mental Health (DZPG), Partner Site Halle-Jena-Magdeburg, Magdeburg, Germany | [30]Department of Behavioral Neurology, Leibniz Institute for Neurobiology, Magdeburg, Germany | [31]Department of Psychology, University of Innsbruck, Innsbruck, Austria | [32]CBBS Center for Behavioral Brain Sciences, Magdeburg, Germany | [33]Institute of Cognitive Neuroscience, University College London, London, UK | [34]Section of Medical Psychology, Department of Psychiatry and Psychotherapy, Faculty of Medicine, University of Bonn, Bonn, Germany

Correspondence: Vanessa Teckentrup (vanessa.teckentrup@tcd.ie)

Received: 27 June 2025 | **Revised:** 10 October 2025 | **Accepted:** 13 October 2025

Keywords: electrical stimulation | MRI | neuroimaging | RF | taVNS | temperature | vagus nerve

ABSTRACT

Background and Purpose: The vagus nerve can be stimulated noninvasively at the ear using transcutaneous auricular vagus nerve stimulation (taVNS). Concurrent functional MRI (fMRI) permits study of taVNS-induced changes in brain dynamics, a key requisite for precision neurostimulation. However, there is no standardized protocol for how to safely apply taVNS during MRI.

Vanessa Teckentrup and Mareike Ludwig shared first authorship.

One major risk is temperature increase exceeding innocuous thresholds due to coupling of the emitted radio frequency (RF) pulse during imaging. Thus, we developed and tested a stimulator cable configuration with floating ground cable traps and filter plate connectors.

Methods: We measured temperature, resonance of the stimulation electrodes, and current interference using unmodified and modified stimulation cables. Measurements were conducted across three sites using different 3T MRI scanner models, stimulators, and stimulation strengths with phantoms and human participants.

Results: The modified compared to the unmodified cable considerably reduced RF heating as the relative temperature increase stayed well below the 2 K threshold specified by the ASTM F2182 standard. Additionally, in accordance with ASTM 2119, we can rule out potential distortion and signal loss around the electrodes due to current flow from the stimulator and demonstrate that impaired image quality in brainstem and midbrain regions is recovered using the modified cable.

Conclusions: We show that adding floating ground cable traps to the stimulator cable allows the safe use of taVNS with fMRI and may improve image quality in functional imaging. To enable other researchers to modify their hardware in the same way, we provide details of the modifications.

1 | Introduction

Transcutaneous stimulation of the auricular branch of the vagus nerve (taVNS) is a promising technique to noninvasively target the vagus nerve, the main pathway connecting visceral organs, including the gut, lungs, and heart, with the nucleus of the solitary tract (NTS) in the brainstem [1]. In contrast to implanted cervical vagus nerve stimulators, taVNS capitalizes on the innervation of the ear by vagal afferents, specifically the auricular branch of the vagus nerve in the cymba conchae and, to a lesser extent, the tragus areas of the outer ear [2]. In recent years, taVNS has gained traction, as vagal signaling has been shown to be implicated in appetitive functions [3], such as reward learning [4], motivation [5], and energy tracking [6], but has also been shown to increase pupil dilation [7] and influence cognitive functions associated with reward seeking [8–10]. Moreover, taVNS has been successfully applied to reduce symptoms in a range of mental health and neurological disorders such as major depressive disorder [11], epilepsy [12–14], and tinnitus [15].

Although a variety of areas have been identified in which taVNS may have beneficial effects, we currently lack insight into how to personalize taVNS treatments to elicit a clinically useful response in most individuals. One of the major challenges in addressing this problem is to isolate the effects of different parameter settings on outcomes of interest (for an overview, see Farmer et al. [16] or Ludwig et al. [17]). The second important area for future research is to uncover the mechanisms of action underlying clinical effects of taVNS. To this end, taVNS can be combined with imaging techniques, such as functional magnetic resonance imaging (fMRI), to explore stimulation- and sensation-related activations along the vagal afferent pathway, including the NTS, and projection regions, such as the locus coeruleus (LC), by comparing active taVNS to sham stimulation [18]. Pioneering work points to increases in brain signaling after taVNS, which was mainly seen throughout the brainstem (i.e., NTS, LC, substantia nigra, dorsal raphe, and periaqueductal gray), but also in the insula, thalamus, nucleus accumbens, putamen, anterior cingulate cortex, and amygdala (see Teckentrup et al. [19] and Ludwig et al. [17] for a review). Common handheld taVNS devices enable the modulation of vagal signal transmission within the magnetic field from a battery-powered stimulator. This stimulator can remain in the control room connected to the earpiece with nonferromagnetic electrodes via a long MR-compatible cable. In the literature to date, the cable connecting the current source to the electrodes was either passed through the waveguide into the scanner room without any further safety-related modifications [20–23] or routed through the radio frequency (RF) filter plate [24, 25]. However, the majority of studies do not provide further details on safety modifications or cable routing, as there is little consensus on which aspects of the setup should be reported [11, 26–37]. One aspect that is not commonly reported is RF energy-induced heating due to the stimulation setup, even though this can be considered an important prerequisite to safely operate electrically powered stimulation devices within the magnetic field of the MRI scanner [38, 39].

For implanted medical devices used within magnetic fields, the American Society for Testing and Materials (ASTM) F2182 standard (applicable at 1.5T and 3T) allows a maximum device-mediated increase in the temperature of the tissue of a human being undergoing an MRI scan of 2 K. Within the RF field of an MRI scanner, such local temperature increases of tissue can result not only from direct deposits of RF energy but also from conductive leads such as the taVNS device cables (for review, see Winter et al. [40]). Coupling between a conductor and the RF transmitting field transforms the lead into a current-carrying antenna, potentially amplifying the heating locally due to RF energy deposition. Human skin acts as a capacitor in this context and can retain the charge, which may lead to burns at the point of contact, that is, where the electrodes are touching the skin [41]. Moreover, the current flow along the cable can generate RF emissions that, similar to susceptibility artifacts, can result in magnetic field inhomogeneities, leading to local geometric distortions or signal loss [42, 43]. Here, the ASTM F2119 standard provides specifications for the experimental setup and the measurement of artifact sizes. Given that there are no specific guidelines for noninvasive stimulation devices, such as those used for taVNS, the ASTM F2119 and F2182 standards—even though developed for passive and implanted devices, which, due to their positioning enclosed by tissue, arguably pose a higher risk [44]—may serve as a sensible reference for the experimental protocols used here. By following these standards, we aim to test the performance of a modified taVNS system in an MR environment.

Taking the criteria laid out in the ASTM F2182 and F2119 standards as a reference, we applied and tested a modification of the stimulator cable. We sought to mitigate the risks of heating and unsafe operation as well as assess the effects of taVNS on MR image quality. We added common-mode suppressing floating ground cable traps that were fixed on the cable with a distance matching the RF wavelength of the respective MRI scanner to reduce the induction of RF currents and, thus, heating along the cable. We incrementally tested the effect of our modification on temperature and image quality based on ASTM F2182-compatible phantoms and human participants at three scanner sites (University of Tübingen [Site 1], University of Magdeburg [Site 2], and University of Bonn [Site 3]) housing different 3T MRI scanners. We modified two commonly used handheld taVNS devices. To further minimize interference with MR imaging, Bayonet Neill–Concelman (BNC) connectors were added to the device cable, allowing routing of the cable through the filter plate of the Faraday cage. Both stimulators were then tested in the active (delivering current) and inactive (switched off) state while we continuously measured the temperature at the electrodes, the cable, and a reference point. During temperature measurements, we ran MR sequences that deposit a high amount of RF power into the tissue, leading to a high specific absorption rate (SAR). Although the change in temperature came close to the threshold of 2 K in measurements based on the unmodified cable, the modification successfully lowered the change in temperature below the threshold, even when setting the stimulation strength to the maximum the device could deliver. Examining artifacts surrounding the electrodes at Site 2, we primarily identified cancellation artifacts. These reached a maximum size of 10.40 ± 1.25 mm, which did not affect signal quality for functional imaging. Extending this observation, functional imaging data acquired from Site 3 in a human participant showed that image quality in the brainstem and midbrain—which was impaired using the unmodified cable—was recovered using the modified cable.

To conclude, modifying the cable of the taVNS stimulator with floating ground cable traps is a viable approach to reduce RF energy-induced heating when applying taVNS during 3T MR imaging. We further demonstrate that our modified setup allows for high-quality imaging as artifacts elicited by the electrodes are small, and the reduced image quality due to distortions in brainstem and midbrain regions with the unmodified cable is recovered with the modification applied. To enable other researchers planning to use taVNS concurrent with fMRI to implement the safety measures reported here, we provide detailed reports of the modifications and refer qualified technical research staff to instructions on how to construct them.

2 | Methods

Measurements of temperature change due to RF energy-induced heating were performed at two sites with the University of Tübingen as Site 1 and the University of Magdeburg as Site 2. Both sites performed measurements using MR-compatible phantoms. Further, at Site 1, measurements with a human participant were conducted. Measurements characterizing distortion and signal loss artifacts linked to the electrodes were performed at Site 2. Additional measurements characterizing distortion and signal loss artifacts in functional imaging of a human brain were performed at the University of Bonn as Site 3. Measurements including human participants received IRB approval from the ethics committees of the University of Tübingen and University of Bonn. All sites used comparable but not identical setups regarding the stimulator, parameters of the modification, and the imaging sequences used, as the measurements reported here were conducted as independent validation efforts of the efficacy of the modification.

2.1 | Stimulation Device

Site 1 used the NEMOS stimulator (tVNS Technologies GmbH, Erlangen, Germany) with two different cables (one unmodified, one modified), each comprising an adjustable earpiece with bipolar titanium electrodes (tVNS Technologies legacy electrode). The earpiece connects to a battery-operated stimulator. For usage within an MRI scanner, MR-compatible cables with an extended length of 7 m were provided by the manufacturer (Figure 1). The device delivers a biphasic signal with a frequency of 25 Hz and a pulse width of 250 μs. The stimulation protocol consists of 30-s OFF and 30-s ON stimulation cycles during which the NEMOS stimulator applies a ramp-up from 0 mA to the selected current strength and a ramp-down back to 0 mA, automatically switching between the phases. The device delivers the desired current independent of skin conductance until a maximum value of 18 kOhm is reached without direct current. The device current setting ranges between 0.1 and 5 mA. This stimulation intensity is typically adjusted on an individual basis prior to commencing the experimental protocol. Frangos et al. [21] observed a range for taVNS current of 0.3–0.9 mA in their taVNS–fMRI study. As heating scales with current strength, we ensured that our method is reflective of the upper stimulation bound in human taVNS, and the current was set to 1.1 mA in all measurements at Site 1. We refer to measurements performed under these conditions at Site 1 as the "Average Load" condition for temperature measurements.

Site 2 used the more recent tVNS R stimulator (tVNS Technologies GmbH, Erlangen, Germany; research-focused version of the tVNS device), with one cable (modified) comprising an adjustable earpiece with bipolar titanium electrodes (tVNS Technologies legacy electrode). The stimulator was connected to a computer in the control room via Bluetooth Low Energy connection, and stimulation parameters could be set individually with a dedicated smartphone application (Figure 2). As Site 2 exclusively used a phantom and the taVNS R stimulator allows more flexible control of stimulation parameters than the NEMOS, we chose a stimulation protocol at the limits of what the stimulation device can deliver to ensure our modification is safe even for the most extreme use case. Hence, the device delivered continuous stimulation with a frequency of 25 Hz, a pulse width of 250 μs, and a current of 5 mA (highest possible intensity setting of the device). We refer to measurements performed under these conditions at Site 2 as the "Maximum Load" condition for temperature measurements.

Measurements at Site 3 were performed using the NEMOS and tVNS R stimulators (both tVNS Technologies GmbH, Erlangen, Germany), with the NEMOS stimulator paired with the modified cable and both the NEMOS and tVNS R stimulators paired with

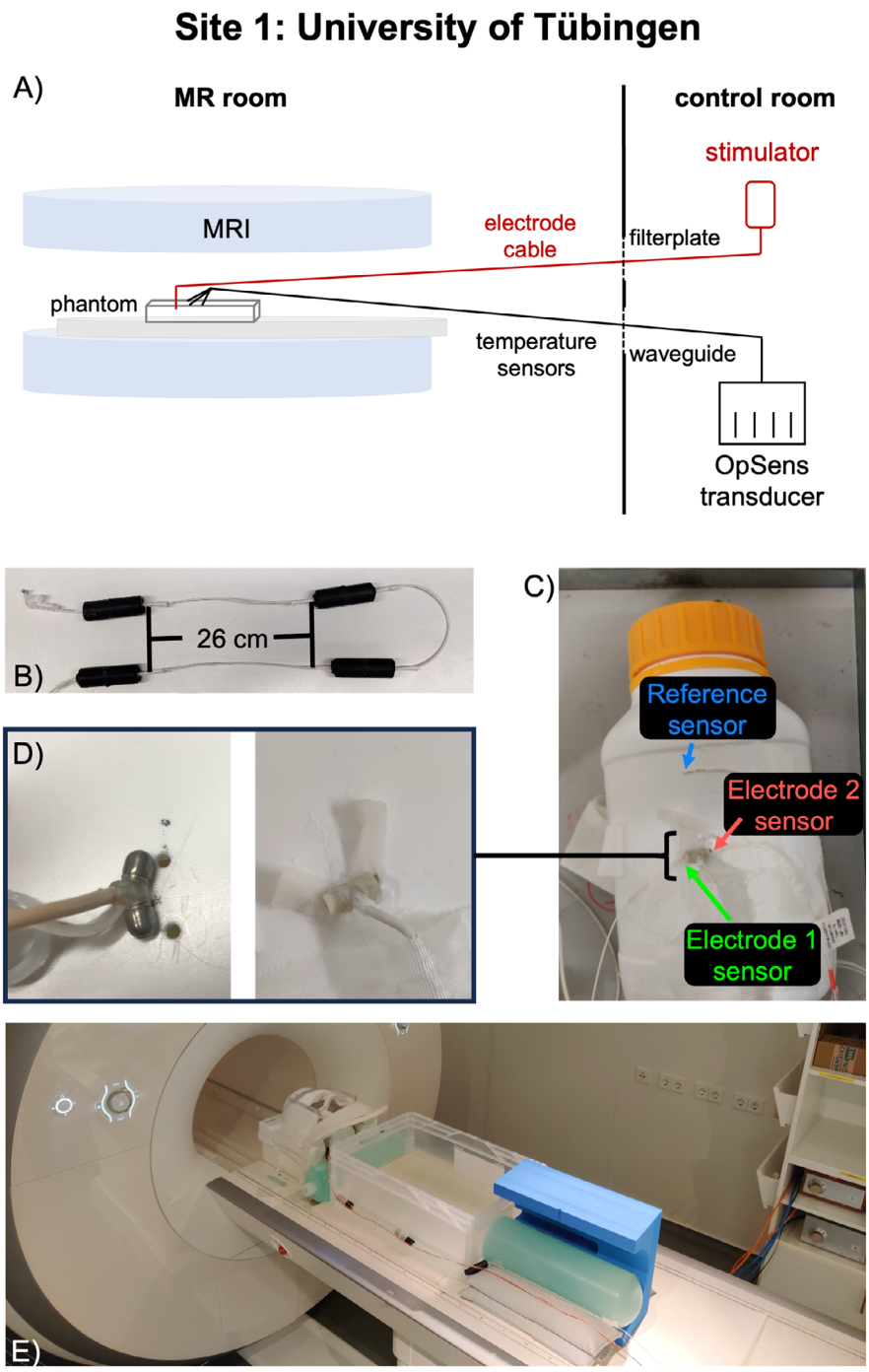

FIGURE 1 | Phantom setup for Site 1 (University of Tübingen). (A) Site 1 used the NEMOS stimulator, fiber optic temperature sensors, and a Siemens Prisma 3T MRI scanner. The stimulator (red box) was placed in the control room with the MR-compatible cable (red line) routed through the filter plate via Bayonet Neill–Concelman connectors (upper dotted black line). Temperature was measured using an OpSens signal transducer (black box) in the control room with three fiber-optic sensors (black line) routed through the waveguide (lower dotted black line). (B) MR-compatible stimulator cable with extended (7 m) length. The cable has been modified with four floating ground cable traps (FCTs), which have been fixed with a 26-cm distance ($\frac{\lambda}{10}$) from each other, matching the 3T radiofrequency wavelength to prevent heating along the cable. (C) Head phantom with two openings to match the distance between the two titanium electrodes of the NEMOS earpiece. At this opening, each electrode comes into contact with the American Society for Testing and Materials (ASTM) 2182 gel (ASTM International) contained within the phantom. (D) Placement of the temperature sensors in relation to the stimulation electrodes. One sensor was placed on the right (Electrode 1) and another on the left (Electrode 2) stimulation electrode. A reference temperature sensor was placed above the electrodes on the head phantom. All sensors were then secured with medical tape. (E) Setup for the phantom-based measurements at Site 1 with (from top to bottom) the head phantom (filled with ASTM 2182 gel) in the 64-channel head coil, two 2-L bottle phantoms to mimic the shoulders, a box filled with ASTM 2182 gel to mimic the torso, and a 5-L bottle phantom to mimic the right leg. For the temperature measurements, stimulation was performed with 30-s ON and 30-s OFF cycles with a frequency of 25 Hz, a pulse width of 250 μs, and a current of 1.1 mA (see Table 1).

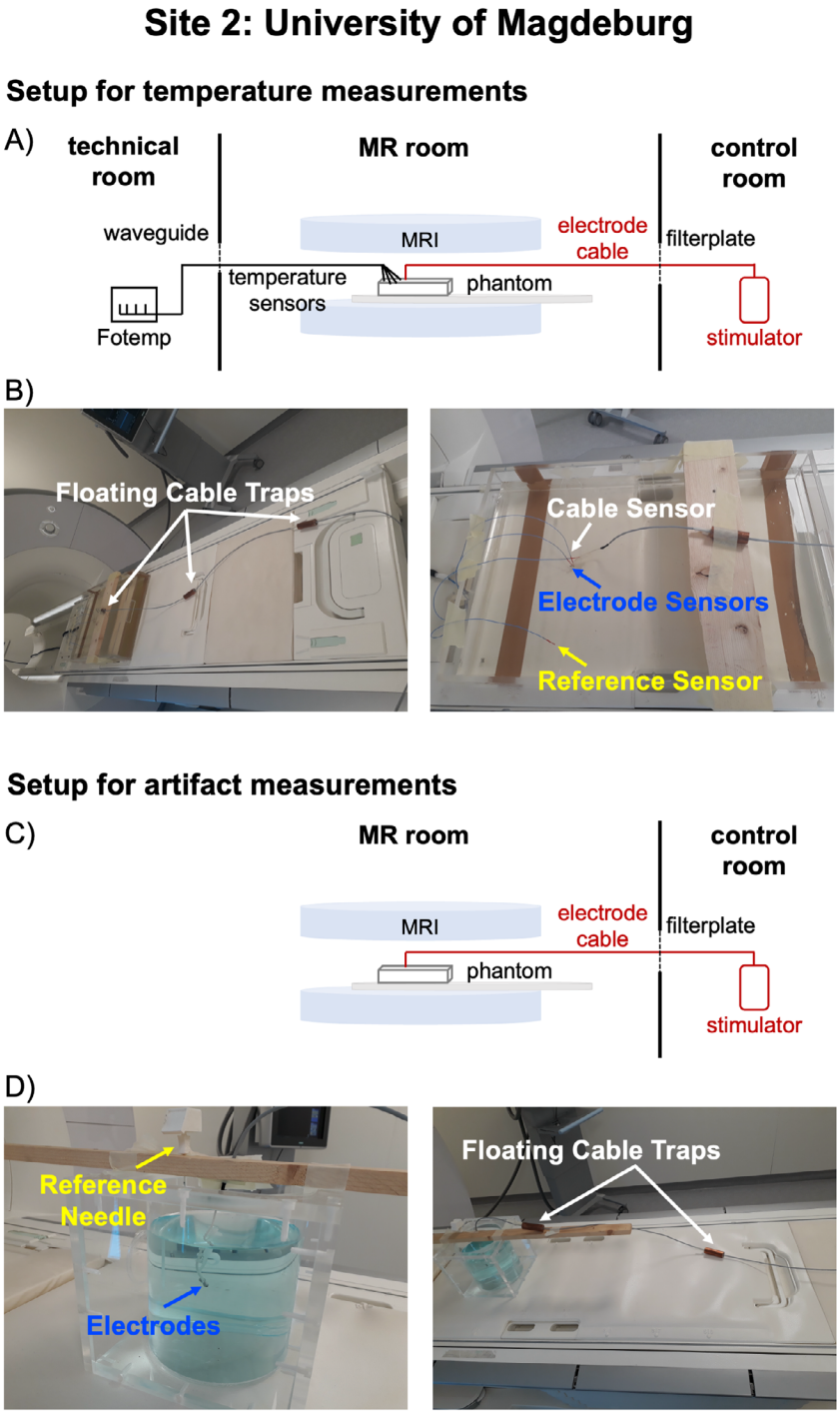

FIGURE 2 | Phantom setup for Site 2 (University of Magdeburg). Site 2 used the tVNS R stimulator with a 3T Siemens Skyra MRI scanner for temperature and artifact measurements. (A) For temperature measurements, the stimulator was placed in the control room, and the MR-compatible cable for the stimulator (electrode cable: red line) was modified with Bayonet Neill–Concelman (BNC) connectors and routed through the filter plate (dotted black line). Temperature measurements were collected using an OPTOcon signal transducer placed in the technical room with four fiber optic temperature sensors that were routed through the waveguide. (B) The left image shows the cable was equipped with three floating ground cable traps fixed with a 60-cm distance ($\frac{\lambda}{4}$) from each other as defined by RF noise measurements (see Section 2.2 for more details). The right image shows the two temperature sensors attached to the two ear electrodes (blue), one temperature sensor attached to the cable (white), and a reference temperature sensor submerged in the phantom (yellow). (C) For artifact measurements, the stimulator was placed in the control room again, and the MR-compatible cable for the stimulator (electrode cable: red line) modified with BNC connectors was routed through the filter plate (dotted black line). (D) The left image shows the two ear electrodes of the stimulator (blue) in the phantom and the ceramic needle (yellow) used as a reference. The right image shows the routing of the modified cable with floating cable traps. For both temperature and artifact measurements, continuous stimulation was performed with a frequency of 25 Hz, a pulse width of 250 μs, and a current of 5 mA (see Table 1).

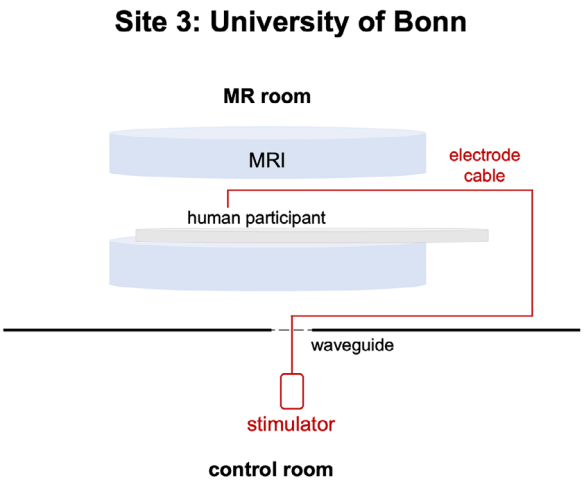

FIGURE 3 | Setup for artifact measurements with a human participant at Site 3 (University of Bonn). Artifact measurements were carried out using a 3T Siemens Trio MRI scanner and NEMOS and tVNS R stimulators with the same modified stimulator cable that was previously used in measurements conducted at Site 1, but another unmodified stimulator cable was used together with the tVNS R stimulator. The stimulator was placed in the control room, and the MR-compatible cable for the stimulator (electrode cable: red line) was routed through the waveguide (broken black line), with the Bayonet Neill–Concelman connectors of the modified cable connected to each other. To prevent heating along the cable in the MR room, four floating ground cable traps were affixed to the cable with a 26-cm distance ($\frac{\lambda}{10}$) from each other. This distance matched the RF wavelength of the 3T MRI scanner (cf. Figure 1). The stimulator earpiece was positioned directly on the ear of the human participant, with the two titanium electrodes placed on the cymba conchae. For the artifact measurements, stimulation was performed with 30-s ON and 30-s OFF cycles with a frequency of 25 Hz, a pulse width of 250 μs, and a current of 0.1 mA (see Table 1).

unmodified cables (Figure 3). While the NEMOS stimulator was paired with the same cables that had previously been used for the measurements performed at Site 1, the tVNS R stimulator was connected to another (unmodified) cable comprising an adjustable earpiece with bipolar titanium electrodes (tVNS Technologies legacy electrode). Site 3 exclusively performed measurements to assess the severity of artifacts in functional imaging of the human brain where the lower stimulation bound was taken to investigate if artifacts can be observed even at the lowest possible current flow. Hence, both stimulators were set to deliver 30-s OFF and 30-s ON stimulation cycles without any ramp-up or ramp-down with a current of 0.1 mA (the lowest intensity setting of the device), a frequency of 25 Hz, and a pulse width of 250 μs. In the results section, we include images for the unmodified cable condition using the tVNS R stimulator. As both stimulators were operated with the same settings and led to comparable levels of artifacts, the images recorded from the NEMOS stimulator paired with the unmodified cable can be regarded as interchangeable.

2.2 | Modifications

For measurements at Site 1 and Site 3, we used two vendor-supplied MR-compatible cables (tVNS Technologies "legacy cable"). One cable was left unmodified, while the second cable was equipped with four floating ground cable traps (FCTs, Figure 4), which were 60 mm in length with a diameter of 20 mm (Figure 1A). The first cable trap was placed as close as practically possible to the earpiece with the titanium electrodes. All remaining cable traps were spread along the cable with a 26-cm distance from each other, that is, spaced about $\frac{\lambda}{10}$ apart, to suppress the common mode and reduce potential heating of the tissue. With the modified setup, all cable traps were located inside the MRI transmit body coil. Following the general design of Seeber et al. [45], each cable trap consisted of an outer and inner conductive cylinder, which were separated by a dielectric Teflon cylindrical support structure and electrically connected at both ends. For this, we first inserted a copper cylinder formed out of 3M adhesive copper tape into the Teflon support structure. Next, we wrapped the entire Teflon structure using a wider adhesive copper tape forming a larger copper cylinder on the outer surface of the Teflon support. Then, the inner and outer copper tapes were soldered together at both ends. After that, we made an incision in the middle of the outer copper cylinder and soldered two chip capacitors separated by 180 degrees in the cut. To ensure maximum attenuation of signal propagation along the outer surface of the cable shield, each cable trap was tuned to the Larmor frequency of the MRI scanner (123.25 MHz) by choosing appropriate values of the two chip capacitors. Also, to tune the traps, two current probes were connected to a vector network analyzer (E 5071C, Agilent Technologies). To protect the outer copper cylinder, each cable trap was covered with heat-shrink tubing. Finally, all cable traps were placed on the MR-compatible (nonferromagnetic) coaxial cable. For this, the cable was cut, resulting in a 2-m-long cable connecting to the stimulator unit. Four cable traps were then placed onto the remaining 5-m-long cable connecting to the stimulator earpiece. Thereafter, a nonmagnetic BNC connector was soldered to each of the bipolar (positive and negative) electrode leads, which allowed us to route the cable through the filter plate of the Faraday cage at Site 1. Both the unmodified and modified cables were reused for measurements at Site 3, which was not equipped with a filter plate. Hence, the BNC connectors of the modified cable (stimulator and earpiece cable segments) were connected to each other, and the cable was routed through the waveguide (Figure 3).

For measurements at Site 2, one vendor-supplied MR-compatible cable was also modified with BNC connectors and routed through the filter plate. The cable was equipped with three FCTs (Figure 4). The first cable trap was fixed at a 32-cm distance from the electrodes as defined by RF noise measurements. The remaining cable traps were fixed with a 60-cm distance from each other, that is, spaced about $\frac{\lambda}{4}$ apart. This distance was chosen to achieve effective RF suppression for the specific conditions of the local MR environment (Table 1). Similar to the design at Site 1, each cable trap consisted of an outer and inner conductor, which were separated by a dielectric support structure and connected via discrete capacitors. The 3D-printed structure was 60 mm in length, with an outer radius of 10 mm and an inner radius of 0.95 mm. Again, the capacitors were chosen so that the FCTs had a resonance at the Larmor frequency of 123 MHz to ensure maximum attenuation of the RF signal.

FIGURE 4 | Floating cable traps (FCTs) were built following Seeber et al. [45]. (A) Each trap featured an inner and outer conductive cylinder, separated by a Teflon dielectric cylindrical support structure and electrically connected at both ends (images show FCTs built for Site 2). FCTs measured 60 mm in length, with a diameter of 20 mm. Capacitors were embedded in the outer cylinder and were tuned to the Larmor frequency of the MRI scanner for maximum attenuation of signal propagation along the outer surface of the cable shield. (B) To protect the outer copper cylinder, each cable trap was covered with heat-shrink tubing (images show FCTs built for Site 1 and Site 3). For measurements at Site 1 and Site 3, the first FCT was placed as close as practically possible to the earpiece with the electrodes. The remaining three cable traps were spread along the cable with a 26-cm distance from each other, that is, spaced about $\frac{\lambda}{10}$ apart. For measurements at Site 2, the first FCT was placed 32 cm from the electrodes, with the remaining traps spaced 60 cm, that is, spaced $\frac{\lambda}{4}$ apart.

2.3 | Setup for Measurements With Phantoms

For temperature measurements at Site 1, we used an ASTM 2182-compliant gel made of polyacrylic acid gelling agent and sodium chloride (NaCl). We included a box to mimic the torso, two 2-L bottle phantoms to mimic the shoulders, and one 5-L bottle phantom to mimic the right leg (Figure 1E). Additionally, a head phantom was filled with ASTM 2182 gel. On the right side of the head phantom are two openings, matching the distance between the two titanium electrode contacts. This positioning mimicked the placement of the stimulation electrodes on the cymba conchae of the ear (Figure 1C). To generate a conductive connection between the electrodes and the gel inside the head phantom, we rolled tissue into two cones, soaked them in the gel, and inserted one cone into each opening. The electrode contacts were secured to the conductive media using tissue-padded medical tape.

For temperature measurements at Site 2, a box filled with an ASTM 2182-compliant gel made of hydroxyethyl cellulose gelling agent and sodium chloride (NaCl) was used. To bring the electrodes of the stimulator unit into contact with the gel, electrodes were lightly immersed in the gel and held in this position by glass fibers fixed to the rim of the box.

Artifact measurements at Site 2 used an additional experimental setup wherein the stimulating electrodes were immersed in a Plexiglas cylinder (height: 16 cm, diameter: 14 cm) filled with cupric sulfate ($CuSO_4$) solution (1.5 g/L, according to ASTM 2119). Electrodes remained fixed at a distance of at least 4 cm from the walls of the cylinder. Additionally, a ceramic needle was inserted into the cylinder to serve as a reference structure to verify artifact size. The body coil was used to record 15 slices covering the entire area around the electrodes.

2.4 | Setup for Measurements With Human Participants

To prevent potential temperature spikes resulting from active stimulation within the scanner from reaching the skin of the

TABLE 1 | Overview of the magnetic resonance imaging setups and technical modifications of the stimulator for transcutaneous auricular vagus nerve stimulation at Site 1 (University of Tübingen), Site 2 (University of Magdeburg), and Site 3 (University of Bonn).

	Site 1 University of Tübingen	Site 2 University of Magdeburg	Site 3 University of Bonn
Stimulation	NEMOS (control room)	tVNS R (control room)	NEMOS/tVNS R (control room)
	30 s ON/OFF	Continuous	30 s ON/OFF
	25 Hz	25 Hz	25 Hz
	250 μs	250 μs	250 μs
	1.1 mA	5 mA	0.1 mA
Scanner	3T Siemens Prisma	3T Siemens Skyra	3T Siemens Trio
Modification	Extended cable (7 m)	Extended cable (13 m)	Extended cable (7 m)
	Four floating cable traps • Fixed with a 26-cm distance from each other	Three floating cable traps • First was fixed at a 32-cm distance • Remaining cable traps have been fixed with a 60-cm distance	Four floating cable traps • Fixed with a 26-cm distance from each other
	BNC connectors	BNC connectors	BNC connectors
	Filter plate	Filter plate	Waveguide
		Computer that can be time-synchronized with stimulation and connected with scanner	
Phantom: temperature measurements	Siemens 64-channel head coil	No head coil	No phantom measurements
	ASTM 2182 gel	ASTM 2182-compliant gel made of hydroxyethyl cellulose gelling agent and natrium chloride	
	Box filled with ASTM 2182 gel, two 2-L bottle phantoms mimicking the shoulders, one 5-L bottle phantom mimicking the right leg		
	Head phantom: holes drilled into the bottle to establish conductive contact between the electrodes and the gel within the phantom	Electrodes were lightly immersed in the gel and held in this position by glass fibers fixed to the rim of the box	
	Sensor 1: right electrode Sensor 2: left electrode Sensor 3: reference, above the electrodes on the phantom	Sensor 1: right electrode Sensor 2: left electrode Sensor 3: cable Sensor 4: reference, placed in the gel of the phantom	
	TSE sequence parameters: • TR: 1.5 s • TE: 0.103 s • Flip angle: 180° • Slices: 18 • Voxel size: 0.8 × 0.8 × 3 mm • FOV: 400 × 400 mm • Matrix size: 256 × 256 • Averages: 3 • Concatenations: 3 • Duration: 6 min	TSE sequence parameters: • TR: 4.82 s • TE: 0.013 s • Flip angle: 169° • Slices: 45 • Voxel size: 2 mm • FOV: 500 × 500 mm • Matrix size: 256 × 256 • Averages: 5 • Duration: 15 min	

(Continues)

TABLE 1 | (Continued)

	Site 1 University of Tübingen	Site 2 University of Magdeburg	Site 3 University of Bonn
	EPI sequence parameters: • TR: 1.4 s • TE: 0.03 s • Flip angle: 65° • Voxel size: 2 mm^3 isotropic • FOV: 220 × 220 mm • Matrix size: 110 × 110 • Multiband factor: 4		
Phantom: artifact measurements	No	Plexiglass cylinder: • Height: 16 cm • Diameter: 14 cm • Filled with cupric sulfate ($CuSO_4$) solution (1.5 g/L, according to ASTM 2119) Fixed electrodes: • Distance of at least 4 cm to the walls of the cylinder Ceramic needle: • Reference structure to verify artefact size Sequence parameters: • Slice thickness: 3 mm • Matrix size: 256 × 256 • FOV: 160 mm • Receiver vs. transmitter coil: body coil SE sequence (*conductivity artefacts*): • TR: 0.1 s • TE: 0.015 s • Flip angle: 90° GRE sequence (*susceptibility artefacts*): • TR: 0.5 s • TE: 0.02 s • Flip angle: 30°	
Human measurements		No measurements in human participants	
	Earpiece connected to the cymba conchae via a plastic tube filled with conductive agar preparation: • 20 mL of purified water • 0.15 g of salt • 0.15 g of agar		Earpiece with electrodes in direct contact with the skin of the cymba conchae

(Continues)

TABLE 1 | (Continued)

Site 1 University of Tübingen	Site 2 University of Magdeburg	Site 3 University of Bonn
TSE sequence parameters: • TR: 1.5 s • TE: 0.103 s • Flip angle: 180° • Slices: 18 • Voxel size: 0.8 × 0.8 × 3 mm • FOV: 400 × 400 mm • Matrix size: 256 × 256 • Averages: 3 • Concatenations: 3 • Duration: 6 min		EPI sequence parameters: • TR: 2.66 s • TE: 0.03 s • Flip angle: 77° • Number of slices: 40 (ascending) • Voxel size: 3 × 3 × 3.3 mm • Matrix size: 64 × 64 • FOV: 192 × 192 mm • Duration: 10 min

Abbreviations: EPI, echo-planar imaging; FOV, field of view; GRE, gradient echo; SE, spin echo; TE, echo time; TR, repetition time; TSE, turbo spin echo.

ear, a conductive agar solution was prepared at Site 1. For this, 20 mL of purified water, 0.15 g of salt, and 0.15 g of agar were mixed in an Erlenmeyer flask, covered with foil, and kept on a hot plate until cooked. The cooled agar preparation was filled into a plastic cylinder with open ends on both sides. One side of the agar tube was then attached to the right cymba conchae of the pilot participant. The titanium electrodes of the stimulator were then attached to the other side of the tube. Thus, current from the activated stimulator could flow due to the conductive preparation, while any potential heating at the electrodes would be prevented from reaching the skin.

Artifact measurements at Site 3 took place after the measurements at Site 1 and Site 2. Hence, safety in terms of potential temperature increases had been established, and the earpiece was placed directly on the ear, with the two titanium electrodes being placed in the cymba conchae.

2.5 | MR Image Acquisition

A full overview of the sequence parameters for all sites is provided in Table 1. MRI data at Site 1 were acquired using a 3T Siemens Prisma scanner (Siemens, Erlangen, Germany) equipped with a 64-channel RF head receiver coil as well as a built-in body transmit coil. To induce a high RF load in the phantom measurements, we used a turbo spin echo (TSE) sequence that ran with 97% of the allowed SAR (TR: 1.5 s, TE: 0.103 s, flip angle: 180°, measurement time: 6 min). To evaluate potential temperature increases within realistic operational conditions for functional measurements, we further used a multiband-accelerated echo-planar imaging (EPI) pulse sequence (University of Minnesota Center for Magnetic Resonance Research, CMRR EPI; TR: 1.4 s, TE: 0.03 s, multiband factor: 4). Finally, we evaluated potential temperature increases for measurements in a human participant using the same TSE sequence described above for phantom-based measurements.

MRI data at Site 2 were acquired using a 3T Siemens Skyra scanner (Siemens, Erlangen, Germany) equipped with the built-in body transmit coil. To induce a high RF load in the phantom measurements, we used a TSE sequence (TR: 4.82 s, TE: 0.013 s, flip angle: 169°, measurement time: 15 min). To capture the full breadth of artifacts in a phantom, we used a spin echo (SE) sequence (TR: 0.1 s, TE: 0.015 s), which is more sensitive to conductivity artifacts, and a gradient echo (GRE) sequence (TR: 0.5 s, TE: 0.02 s), which is more sensitive to susceptibility artifacts.

MRI data at Site 3 were acquired using a 3T Siemens Trio scanner (Siemens, Erlangen, Germany) equipped with a 32-channel RF head receiver coil as well as a built-in body transmit coil. To evaluate artifacts due to current flow along the stimulator cable within realistic operational conditions for measurement in a human participant, we used an EPI sequence (TR: 2.66 s, TE: 0.03 s, flip angle: 77°, measurement time: 10 min) with 40 slices covering the whole brain.

2.6 | Phantom fMRI–taVNS for Temperature Measurements

For Site 1, we acquired a 10-min reference measurement without an active sequence to evaluate baseline temperature fluctuations of the electrodes within the static magnetic field. After this, we ran a localizer and positioned the slices over the electrodes attached to the phantom. Then, we acquired a 2-min baseline measurement before running the TSE sequence for 7 min, followed by another 2 min of baseline recording. This measurement was then repeated with an active current running through the cable. For this, we set the stimulator to 1.1 mA and activated the stimulation prior to starting the 2-min baseline recording.

For Site 2, we first acquired a 20-min reference measurement without an active sequence to evaluate baseline temperature fluctuations of the electrodes within the static magnetic field. After this, we ran the TSE sequence for 15 min without active stimulation, followed by a third measurement block of 15 min with 5 mA continuous stimulation during TSE sequence acquisition. For brevity, we only detail the sequences underlying the results reported in the main text here. The full list of MR sequences and the respective temperature trajectories can be found in Table 1.

2.7 | Human taVNS–fMRI

At Site 1, we first acquired a 2-min reference measurement without an active sequence to evaluate baseline temperature fluctuations of the electrodes within the static magnetic field. Then, we ran a localizer and positioned the slices over the cymba conchae of the ear before starting the stimulation, with the current intensity set to 1.1 mA. Finally, during active stimulation, we acquired a 2-min baseline measurement before running the TSE sequence for 7 min, followed by another 2 min of cool-down recording.

At Site 3, we ran a localizer and positioned the slices to cover the full brain before starting the stimulation, with the current intensity set to 0.1 mA. We ran the EPI sequence for 10 min, once with the unmodified cable and once with the modified cable.

2.8 | Temperature Measurements

To measure temperature at Site 1, we used an OpSens temperature signal transducer and three fiber optic temperature sensors. Temperature was recorded using SoftSens version 2.23.0 (Opsens Solutions, Québec, Canada). For phantom-based measurements, we attached one sensor to each of the titanium electrodes of the stimulator, while the third sensor was placed above the electrodes on the phantom and served as a reference (Figure 1B). Padded electrode covers, provided by the manufacturer, were soaked in ASTM 2182 gel and used to firmly position the temperature sensors to the electrodes. All cables (for stimulation and temperature recording) were placed along the right side of the phantom at the level of the ear's cymba conchae (Figure 1D). For measurements in the human participant, the reference sensor was placed on the sheet that was covering the participant, on the left side of the upper body. The other two sensors were attached to each of the titanium electrodes (i.e., identical to the phantom measurements). For each temperature sensor, we determined the temperature offset (left electrode: 1 K, right electrode: 0.5 K, reference: 1.1 K). During measurements, we accounted for all offsets in the SoftSens recording software.

Site 2 used an OPTOcon GmbH FOTEMP4-16 temperature signal transducer with four fiber optic temperature sensors. One sensor was attached to each of the titanium electrodes of the stimulator unit (Figure 2A). A third sensor was attached to the cable, while a fourth sensor, placed in the gel of the phantom, served as the reference.

To obtain accurate values for maximum temperature increase at the electrodes for each measurement condition, we corrected the time series of temperature readouts for different sources of drift in our analyses. To account for baseline temperature in each channel, we used the baseline measurements acquired within the static magnetic field (without an active sequence or stimulation) and subtracted the average baseline temperature of each channel from the respective channel's measurements derived under Average and Maximum Load conditions. To further account for slow drifts in the temperature of the ASTM 2182 gel over time, we used the temperature measurements derived from the reference channel in each measurement condition and ran a linear regression predicting the trajectory of temperature measurements in this channel by time to capture slow linear increases. We then subtracted the predicted values from each channel to obtain the final temperature trajectories.

2.9 | Characterization of Artifacts

Distortion and signal loss artifacts from the titanium electrodes could affect the MR signal in brain regions of interest, including brainstem nuclei located about 4 cm from the electrodes. Therefore, we performed additional artifact measurements at Site 2. Artifacts were evaluated according to ASTM 2119 standard specifications. This resulted in collecting the following: (1) MR image of the phantom with reference structure, without test object; (2) MR image of the phantom with reference structure and test object (switched off); (3) MR image of the phantom with reference structure and test object (continuous stimulation, 5 mA); and (4) repetition of all images with reversed phase/read encoding direction. First, we calculated difference images by subtracting the reference images from those with the electrodes and normalized these images to the reference. To boost edge detection, all voxels with an intensity <0.3 were set to zero and all voxels with an intensity ≥0.3 were set to 1. The electrodes were approximated as cylinders with dimensions of 3.9×11.75 mm^2, and the artifact diameter was determined by measuring the distance between the edge of the electrodes and the last voxel of the artifact in the MR images. Then, the electrode size was subtracted from the artifact diameter. For each sequence separately, we took the largest value based on this method as the artifact size. Given the sequence parameters, reported artifact sizes include an uncertainty of $2 \times \frac{160\ \text{mm}}{256} = 1.25\text{mm}$.

3 | Results

3.1 | Temperature Measurements Across Conditions and Stimulation Current Loads

Using a TSE sequence and active stimulation prior to modifications with an average stimulation strength of 1.1 mA applied to a phantom (data from Site 1), we measured the highest overall maximum temperature increase of 1.95 K (Figure 5A). With the FCTs added to the stimulator cable (Site 1, Average Load condition), we measured a maximum temperature increase of 0.1 K (Δ max. temperature $_{\text{modified – unmodified}} = -1.86$ K; Figure 5C). Using a similar TSE sequence (see Table 1), a stimulator cable equipped with FCTs, and active stimulation at the maximum stimulation strength of 5 mA (Site 2, Maximum Load condition) applied to a phantom, the maximum temperature increase was 1.51 K (Δ max. temperature$_{\text{modified – unmodified}} = -0.44$ K; Figure 5B). Using the same sequence, a stimulator cable equipped with FCTs, and active stimulation at the average stimulation strength of 1.1 mA (Site 1, Average Load condition) applied to the human ear, we measured the overall lowest maximum temperature increase of 0.06 K (Δ max. temperature $_{\text{modified – unmodified}} = -1.89$ K; Figure 5D). To assess potential temperature increases within realistic operational conditions for functional measurements, we also measured temperature increase using a multiband-accelerated EPI sequence, a stimulator cable equipped with FCTs, and active stimulation at the average stimulation strength of 1.1 mA (Site 1, Average Load condition) applied to a

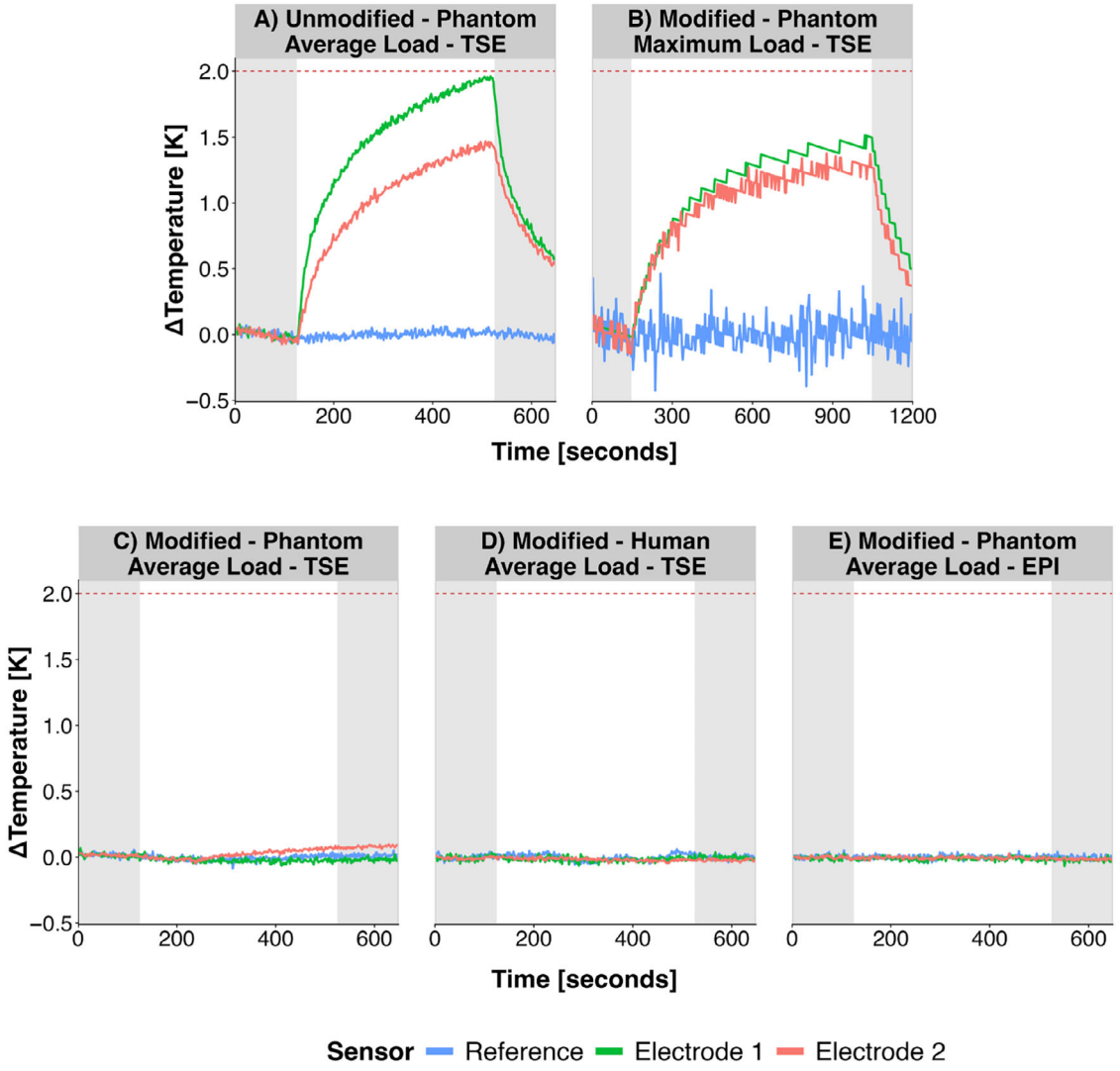

FIGURE 5 | Modification of the cable attenuates the stimulation-induced temperature increase. All panels show temperature relative to the start of the measurement in K for the right (Electrode 1, green), left (Electrode 2, red), and reference (blue) temperature sensors. Areas shaded in gray mark periods during which no active sequence was run. White areas reflect the active turbo spin echo (TSE, A–D) or echo-planar imaging (EPI, E) sequence. The temperature change in Electrode 1 approaches the limit of a 2-K increase (red dashed line) for the unmodified cable (A), but the maximum temperature increase for the modified cable under maximum load (5 mA) was 1.51 K (B). Under average load (1.1 mA), none of the temperature change trajectories for the modified cable exceed an increase of 0.1 K. This is true for both a turbo spin echo sequence in phantom-based (C) or human-based measurements (D), and for measurements using an echo-planar imaging sequence in a phantom (E).

phantom and found a maximum temperature increase of 0.03 K (Figure 5E).

3.2 | Phantom-Based Assessment of Artifacts at the Stimulation Electrodes

For the GRE sequence with no active stimulation, we observed a maximum artifact size of 10.4 mm (±1.25 mm). With active stimulation (continuous stimulation, 5 mA), the maximum artifact size was 10.1 mm (±1.25 mm) and fell within the range of uncertainty for the measurement. Hence, active stimulation did not affect the size of the artifact (Figure 6). For the SE sequence without active stimulation, we observed an overall smaller maximum artifact size of 4.9 mm (±1.25 mm). With active stimulation, observed artifacts increased in size, with a maximum artifact size of 5.9 mm (±1.25 mm), once again falling within the range of uncertainty for the measurement.

3.3 | Assessment of taVNS Artifacts During Functional Imaging of the Human Brain

With the unmodified cable and stimulation intensity set to 0.1 mA, we observed distortions in mid- and hindbrain regions containing main areas of interest for taVNS research such as NTS, LC, or the dopaminergic midbrain. Using the modified cable and the same stimulation intensity setting of 0.1 mA, image quality was recovered in all areas previously affected (Figure 7A). We calculated temporal signal-to-noise ratio (tSNR) for the intracranial volume to quantify the extent of distortion. For functional MR data acquired using the unmodified cable,

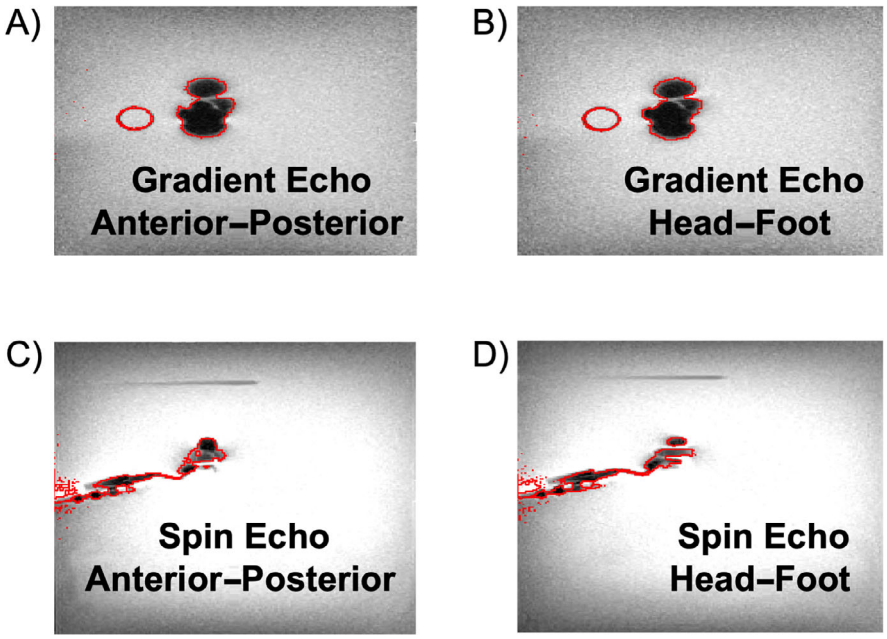

FIGURE 6 | Modification of the cable does not affect image quality. The ear electrodes were examined at Site 2 (University of Magdeburg) according to standard testing methods for evaluation of MR image artifacts from passive implants (ASTM 2119, ASTM International) with and without active taVNS stimulation (continuous stimulation, 5 mA). The increase in artifact size from inactive to active stimulation is marked in red. The extent of artifacts was measured concurrent to gradient echo (A and B) and spin echo (C and D) sequence acquisition. ASTM, American Society for Testing and Materials.

we measured a mean tSNR of 77.74 (range = 5.86–304.81), which was well below the mean tSNR of 145.30 (range = 4.94–515.89) measured using the cable modified with FCTs (Figure 7B).

4 | Discussion

To explore more precise neurostimulation applications in research and for clinical applications, investigating the effects of taVNS on changes in brain activation with fMRI has rapidly gained traction [3, 25, 32, 35, 46]. However, a current lack of detailed guidelines on how to safely implement concurrent taVNS–fMRI without harming people or equipment precludes the widespread use of this technique by imposing unnecessary burden for the approval of new studies. Therefore, we present a modification for an fMRI–taVNS setup that prevents excessive RF-induced heating and reduces MR artifacts to a level that poses no threat to image quality in taVNS–fMRI studies.

Fixing RF chokes to cables operating within RF transmitting fields, such as the MR environment, is a standard approach to attenuate RF current flow, resulting in reduced heating of the component and an improved signal-to-noise ratio [47]. However, the retroactive fitting of RF chokes to commercial devices is commonly seen as difficult because the chokes need to be in direct electrical contact with the cable shield. To this end, the protective coating needs to be opened, which can lead to loss of manufacturer approval. In contrast, FCTs do not require a direct electrical connection while still attenuating the RF frequencies in the MRI's spectrum [48, 49]. Following the instructions in Seeber et al. [45], FCTs can easily be produced by qualified technical research staff and can be freely positioned on the cable to match the specific RF wavelength of an MRI scanner. Hence, FCTs are easily adaptable to local MRI setups and solve common problems with approval when attempting to retroactively modify commercial stimulation devices for improved reduction of RF-induced currents and subsequent heating of components.

To assess the effectiveness of our modification in reducing RF-induced heating at the electrodes of a transcutaneous vagus nerve stimulation device, we ran temperature measurements in phantoms and a human participant contrasting unmodified and modified stimulator cables under different stimulation strengths. Approaching the limit of a 2-K temperature increase specified by the ASTM F2182 standard, we observed a maximum temperature increase of 1.95 K in the unmodified cable under the Average Load condition using a phantom. In this condition, the stimulator was producing a stimulation strength of 1.1 mA, which is commonly used in behavioral taVNS studies [21]. As expected, adding FCTs to the cable resulted in decreased heating. Compared to the unmodified cable, we observed a 95% decrease in RF-induced heating using a phantom and a 97% decrease for the human participant.

Still, as the stimulator produces a maximum stimulation strength of 5 mA, it cannot be ruled out that higher stimulation intensities would exceed the threshold of 2 K. However, operating the stimulator at the maximum stimulation strength of 5 mA with FCTs attached in a phantom resulted in a temperature increase of 1.51 K, which was 22% lower than what we observed using the unmodified cable under average load and well below the threshold laid out in the ASTM F2182 standard. It is important to note that the setups differed in terms of the MRI scanner models, specific sequence parameters, and the number of FCTs added to the stimulator cable between Site 1 and Site 2, as the exact specification needs to be tailored to the local MR environment. For example, Site 2 used three FCTs spaced $\lambda/4$ apart, while Site 1 used four FCTs spaced $\lambda/10$ apart. The observed difference in

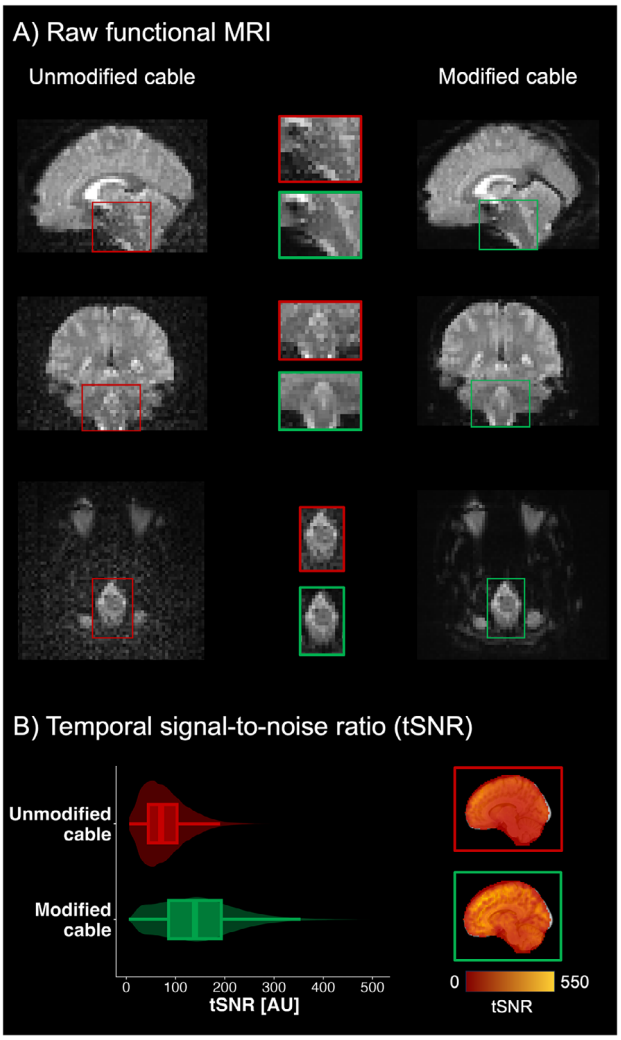

FIGURE 7 | Modification of the cable attenuates distortions in mid- and hind-brain regions. (A) Artifacts in functional MR imaging were assessed by comparing an unmodified cable to a modified cable equipped with floating cable traps at Site 3 (University of Bonn). With the stimulation strength set to 0.1 mA (lowest possible setting of the stimulator) and using the unmodified cable (left column), distortions (red-framed insets) affected mid- and hind-brain regions, including target regions relevant for human taVNS research such as the nucleus tractus solitarius, locus coeruleus, thalamus, or dopaminergic midbrain. Using the same stimulation setting with the modified cable (right column), distortions in the same areas were attenuated, and image quality was restored (green-framed insets). (B) Calculating temporal signal-to-noise ratio to quantify the extent of distortion, we found a mean temporal signal-to-noise ratio (tSNR) of 77.74 (range = 5.86–304.81) for the unmodified cable (red), which was well below the mean tSNR of 145.30 (range = 4.94–515.89) measured using the cable modified with floating cable traps (green). The insets on the right side show the respective tSNR maps overlayed on a standard brain in MNI space.

heating between the sites could be due to these differences in FCT configuration as well as the stimulation settings used at Site 2 (5 vs. 1.1 mA), which might have led to increased resistance in Site 2. Still, adding FCTs to the stimulator cable compared to using a nonmodified, vendor-supplied cable resulted in a stimulation-induced temperature increase below the relevant 2 K threshold at both sites.

While we acquired most of our measurements using a TSE sequence with high RF load, we also assessed phantom-based temperature changes for an EPI sequence, which is more commonly used in functional neuroimaging studies. Crucially, for this use case, which is closer to realistic operational conditions, we observed the lowest temperature increase of 0.03 K. We conclude that our modification results in a reliable reduction of RF-induced heating below the critical threshold of 2 K, with the most substantial reduction in heating recorded for an EPI sequence that is most commonly used in taVNS–fMRI.

To successfully measure taVNS-induced changes in brain signaling, limiting the size of MR artifacts resulting from the stimulation electrodes is decisive, as early studies passing the cable through the waveguide without further modifications reported clear interactions between the setup and RF field, resulting in visible artifacts [21, 23]. Core brain regions of interest for taVNS, such as NTS [50] or LC [51, 52], are located in the brainstem, about 40 mm from the electrodes. Hence, we first assessed the size of MR artifacts at the earpiece of the stimulator following the ASTM 2119 standard specifications. Using the modified cable with the maximum stimulation strength of 5 mA, we compared the active stimulation condition with no stimulation and observed a maximum artifact size of 10.4 mm. This is well below the 40 mm characterizing the distance to brain areas of interest, even when taking the measurement uncertainty of 1.25 mm into account. Importantly, we tested for two common sources of MRI artifacts from metallic objects: (1) conductivity artifacts, or local magnetic field distortions due to additional magnetic field gradients induced by the interaction between rapidly changing magnetic field gradients and conductive materials, and (2) susceptibility artifacts referring to distortions or signal loss due to profound differences in the degree to which a material itself is magnetized in the magnetic field of the MRI scanner [53]. We employed both SE and GRE sequences to fully evaluate the potential for artifacts, as these sequences show different sensitivities regarding the two artifact types [54, 55].

Still, EPI sequences with multiband acceleration—which are more commonly used in functional MRI studies—can show a further increased sensitivity to susceptibility artifacts due to their rapid acquisition of multiple *k*-space lines during a single echo acquisition [56–58]. Here, we calculated tSNR for the unmodified compared to the modified stimulator cable based on functional MRI recordings using an EPI sequence and active stimulation in Site 3 (tSNR maps are available from: https://neurovault.org/collections/WWPOEHQQ/). The mean tSNR nearly doubled across the intracranial volume when going from the unmodified cable (mean tSNR = 77.74) to the cable fitted with FCTs (mean tSNR = 145.30). As the network of brain regions linked to the NTS in the hindbrain extends toward midbrain and cortical areas [3, 21], we further tested for MR artifacts induced by the active stimulation in these downstream regions. Both hind- and mid-brain regions were affected by substantial distortions when using the unmodified cable, even with the stimulator set to the lowest current strength available (0.1 mA). Using the modified cable, distortions were attenuated, and image quality was restored. Importantly, in contrast to the measurements analyzing artifacts around the stimulation electrode, we compared the modified to the unmodified cable under active stimulation here, which

provides an explanation for the greater difference in artifacts observed here. While active compared to no stimulation increases artifact size slightly, our data indicate that adding FCTs to the stimulator cable compared to using a nonmodified cable has a far greater positive impact regarding the minimization of MR artifacts. In sum, with our modified setup, artifacts around the electrodes of the stimulator are small and pose no threat to image quality, especially with the modification further attenuating distortions in key regions of interest in a taVNS–fMRI study.

While the modification performed to our expectations, regarding the reduction of RF-induced heating and the control of MR artifacts, we would like to make researchers interested in adapting this modification for their own setup aware of a few limitations. First, we did not test the extent to which the set stimulation parameters translate to the electrode contacts during imaging, as the modification could alter the current strength that reaches the electrodes. This could be tested by connecting a resistor to each electrode and continuously recording the current reaching the electrodes using an oscilloscope. In taVNS studies, the stimulation strength is typically set individually, using a stepwise procedure to identify the setting that results in a subjective experience of mild, nonpainful prickling. In our previously published registered report, which used the modified stimulator cable [19], we did observe higher average stimulation strengths (sham stimulation: M [range] = 3.69 [2.4–5] mA; taVNS: M [range] = 3.59 [1.5–5] mA) compared to Frangos et al. [21]. While the nature of our data does not determine the primary mechanism contributing to the temperature increase, the data indicate that our modification results in a safe setup, even when the maximum stimulation strength of 5 mA is applied. Likewise, using the stepwise procedure ensures the same subjective experience during stimulation, even if the current generated by the current source needs to be increased due to losses along the cable that could be induced by the modification. Second, we would like to point out that due to the independent nature of the validation attempts, we only performed the temperature measurements in a human participant using the Average Load setting. Still, given that in all conditions the temperature was measured at the electrode, which is the main point of contact between the material suffering from RF-induced heating and the human skin, we would expect a similar trajectory of temperature increase between the phantom and a human participant when the modified cable is used. Third, all measurements were performed using 3T MRI scanners and taVNS stimulators with a predefined range of current loads that have been established as the gold standard in the field. The trajectories of temperature change as well as artifact occurrence might differ in higher field strengths or with higher current loads that can be provided by general transcutaneous electrical nerve stimulation devices. As the capacitors in the FCTs are commonly tuned to the Larmor frequency of the local MRI scanner, our modification can be tailored to other setups including MRI scanners with higher field strengths [59], so independent groups can implement the same modification before verifying that changes in temperature and the extent of artifacts are still within safe limits.

Taken together, we show that adding FCTs to the cable connecting a taVNS stimulator with the electrodes (1) reduces RF-induced heating back to safe levels, (2) does not add artifacts around the electrodes that could hamper image quality, and (3) even improves the signal-to-noise ratio in hind- and midbrain regions of interest for taVNS–fMRI studies. FCTs are easy to produce by qualified technical research staff following published guidelines and can be installed on the cable without opening the coating, thus preserving manufacturer approval. Hence, our modification enables the safe use of taVNS with fMRI while simultaneously improving functional neuroimaging quality.

Acknowledgments

We thank Matthias Arndt for his technical support on modifying the stimulator cable at Site 1.

This work was supported by a University of Tübingen, Faculty of Medicine fortüne grant (#2453-0-0). V.T. is supported by a Government of Ireland Postdoctoral Fellowship (GOIPD/2023/1238). J.S. and O.S. are supported by the Federal Ministry of Education and Research within the Research Campus STIMULATE (13GW0473A, 13GW0473B). O.S. is supported by the Sonderforschungsbereich 1315, Project B06, Sonderforschungsbereich 1436, Project Z02, and DFG core facility INST272/340-1. R.H. is supported by the National Institutes of Health (NIH) NIMH Project P50MH109429. H.P. is supported by a grant (01GI0925) from the Federal Ministry of Education and Research (BMBF) to the German Center for Diabetes Research (DZD e.V.). D.H. is supported by Sonderforschungsbereich 1315, Project B06, Sonderforschungsbereich 1436, Project A08, ARUK SRF2018B-004, and NIH R01MH126971. B.P. is supported by a H2020 FET-Open AROMA grant (agreement no. 885876; NWO TTW 016.Vidi.178.052). H.I.L.J. is supported by the NIH NIA (R01AG062559, R01AG068062, R01AG082006, R21AG074220) and the Alzheimer's Association (AARG-22-920434). N.B.K. is supported by the German Research Foundation (DFG), grants KR 4555/7-1, KR 4555/9-1, and KR 4555/10-1.

Disclosure

This work was previously published as a preprint on the Open Science Framework (https://doi.org/10.31234/osf.io/w6htx_v1).

Conflicts of Interest

The authors declare no conflicts of interest.

References

1. H. R. Berthoud and W. L. Neuhuber, "Functional and Chemical Anatomy of the Afferent Vagal System," *Autonomic Neuroscience* 85 (2000): 1–17, https://doi.org/10.1016/S1566-0702(00)00215-0.

2. M. F. Butt, A. Albusoda, A. D. Farmer, and Q. Aziz, "The Anatomical Basis for Transcutaneous Auricular Vagus Nerve Stimulation," *Journal of Anatomy* 236 (2020): 588–611, https://doi.org/10.1111/joa.13122.

3. V. Teckentrup and N. B. Kroemer, "Mechanisms for Survival: Vagal Control of Goal-Directed Behavior," *Trends in Cognitive Sciences* 28 (2024), 237–251, https://doi.org/10.1016/j.tics.2023.11.001.

4. A. Kühnel, V. Teckentrup, M. P. Neuser, et al., "Stimulation of the Vagus Nerve Reduces Learning in a Go/No-Go Reinforcement Learning Task," *European Neuropsychopharmacology* 35 (2020): 17–29, https://doi.org/10.1016/j.euroneuro.2020.03.023.

5. M. P. Neuser, V. Teckentrup, A. Kuhnel, M. Hallschmid, M. Walter, and N. B. Kroemer, "Vagus Nerve Stimulation Boosts the Drive to Work for Rewards," *Nature Communications* 11 (2020): 3555, https://doi.org/10.1038/s41467-020-17344-9.

6. G. H. Vijgen, N. D. Bouvy, L. Leenen, et al., "Vagus Nerve Stimulation Increases Energy Expenditure: Relation to Brown Adipose Tissue Activity," *PLoS ONE* 8 (2013): e77221, https://doi.org/10.1371/journal.pone.0077221.

7. O. Sharon, F. Fahoum, and Y. Nir, "Transcutaneous Vagus Nerve Stimulation in Humans Induces Pupil Dilation and Attenuates Alpha Oscillations," *Journal of Neuroscience* 41 (2021): 320–330, https://doi.org/10.1523/JNEUROSCI.1361-20.2020.

8. K. B. Clark, D. K. Naritoku, D. C. Smith, R. A. Browning, and R. A. Jensen, "Enhanced Recognition Memory Following Vagus Nerve Stimulation in Human Subjects," *Nature Neuroscience* 2 (1999): 94–98, https://doi.org/10.1038/4600.

9. H. I. Jacobs, J. M. Riphagen, C. M. Razat, S. Wiese, and A. T. Sack, "Transcutaneous Vagus Nerve Stimulation Boosts Associative Memory in Older Individuals," *Neurobiology of Aging* 36 (2015): 1860–1867, https://doi.org/10.1016/j.neurobiolaging.2015.02.023.

10. A. N. Suarez, T. M. Hsu, C. M. Liu, et al., "Gut Vagal Sensory Signaling Regulates Hippocampus Function Through Multi-Order Pathways," *Nature Communications* 9 (2018): 2181, https://doi.org/10.1038/s41467-018-04639-1.

11. J. Fang, N. Egorova, P. Rong, et al., "Early Cortical Biomarkers of Longitudinal Transcutaneous Vagus Nerve Stimulation Treatment Success in Depression," *NeuroImage Clinical* 14 (2017): 105–111, https://doi.org/10.1016/j.nicl.2016.12.016.

12. T. R. Henry, R. A. Bakay, J. R. Votaw, et al., "Brain Blood Flow Alterations Induced by Therapeutic Vagus Nerve Stimulation in Partial Epilepsy: I. Acute Effects at High and Low Levels of Stimulation," *Epilepsia* 39 (1998): 983–990, https://doi.org/10.1111/j.1528-1157.1998.tb01448.x.

13. R. H. Howland, "Vagus Nerve Stimulation," *Current Behavioral Neuroscience Reports* 1 (2014): 64–73, https://doi.org/10.1007/s40473-014-0010-5.

14. H. Stefan, G. Kreiselmeyer, F. Kerling, et al., "Transcutaneous Vagus Nerve Stimulation (t-VNS) in Pharmacoresistant Epilepsies: A Proof of Concept Trial," *Epilepsia* 53 (2012): e115–e118, https://doi.org/10.1111/j.1528-1167.2012.03492.x.

15. N. Yakunina and E. C. Nam, "Direct and Transcutaneous Vagus Nerve Stimulation for Treatment of Tinnitus: A Scoping Review," *Frontiers in Neuroscience* 15 (2021): 680590, https://doi.org/10.3389/fnins.2021.680590.

16. A. D. Farmer, A. Strzelczyk, A. Finisguerra, et al., "International Consensus Based Review and Recommendations for Minimum Reporting Standards in Research on Transcutaneous Vagus Nerve Stimulation (Version 2020)," *Frontiers in Human Neuroscience* 14 (2020): 568051, https://doi.org/10.3389/fnhum.2020.568051.

17. M. Ludwig, C. Wienke, M. J. Betts, T. Zaehle, and D. Hammerer, "Current Challenges in Reliably Targeting the Noradrenergic Locus Coeruleus Using Transcutaneous Auricular Vagus Nerve Stimulation (taVNS)," *Autonomic Neuroscience* 236 (2021): 102900, https://doi.org/10.1016/j.autneu.2021.102900.

18. M. Ludwig, C. Pereira, M. Keute, E. Duzel, M. J. Betts, and D. Hammerer, "Evaluating Phasic Transcutaneous Vagus Nerve Stimulation (taVNS) With Pupil Dilation: The Importance of Stimulation Intensity and Sensory Perception," *Scientific Reports* 14 (2024): 24391, https://doi.org/10.1038/s41598-024-72179-4.

19. V. Teckentrup, M. Krylova, H. Jamalabadi, et al., "Brain Signaling Dynamics After Vagus Nerve Stimulation," *NeuroImage* 245 (2021): 118679, https://doi.org/10.1016/j.neuroimage.2021.118679.

20. S. Dietrich, J. Smith, C. Scherzinger, et al., "A Novel Transcutaneous Vagus Nerve Stimulation Leads to Brainstem and Cerebral Activations Measured by Functional MRI," *Biomedizinische Technik Biomedical Engineering* 53 (2008): 104–111, https://doi.org/10.1515/BMT.2008.022.

21. E. Frangos, J. Ellrich, and B. R. Komisaruk, "Non-Invasive Access to the Vagus Nerve Central Projections via Electrical Stimulation of the External Ear: fMRI Evidence in Humans," *Brain Stimulation* 8 (2015): 624–636, https://doi.org/10.1016/j.brs.2014.11.018.

22. E. Frangos and B. R. Komisaruk, "Access to Vagal Projections via Cutaneous Electrical Stimulation of the Neck: fMRI Evidence in Healthy Humans," *Brain Stimulation* 10 (2017): 19–27, https://doi.org/10.1016/j.brs.2016.10.008.

23. T. Usichenko, R. Laqua, B. Leutzow, and M. Lotze, "Preliminary Findings of Cerebral Responses on Transcutaneous Vagal Nerve Stimulation on Experimental Heat Pain," *Brain Imaging and Behavior* 11 (2017): 30–37, https://doi.org/10.1007/s11682-015-9502-5.

24. B. W. Badran, L. T. Dowdle, O. J. Mithoefer, et al., "Neurophysiologic Effects of Transcutaneous Auricular Vagus Nerve Stimulation (taVNS) via Electrical Stimulation of the Tragus: A Concurrent taVNS/fMRI Study and Review," *Brain Stimulation* 11 (2018): 492–500, https://doi.org/10.1016/j.brs.2017.12.009.

25. R. G. Garcia, R. L. Lin, J. Lee, et al., "Modulation of Brainstem Activity and Connectivity by Respiratory-Gated Auricular Vagal Afferent Nerve Stimulation in Migraine Patients," *Pain* 158 (2017): 1461–1472, https://doi.org/10.1097/j.pain.0000000000000930.

26. D. Borgmann, L. Rigoux, B. Kuzmanovic, et al., "Technical Note: Modulation of fMRI Brainstem Responses by Transcutaneous Vagus Nerve Stimulation," *Neuroimage* 244 (2021): 118566, https://doi.org/10.1016/j.neuroimage.2021.118566.

27. J. Fang, P. Rong, Y. Hong, et al., "Transcutaneous Vagus Nerve Stimulation Modulates Default Mode Network in Major Depressive Disorder," *Biological Psychiatry* 79 (2016): 266–273, https://doi.org/10.1016/j.biopsych.2015.03.025.

28. T. Kraus, K. Hosl, O. Kiess, A. Schanze, J. Kornhuber, and C. Forster, "BOLD fMRI Deactivation of Limbic and Temporal Brain Structures and Mood Enhancing Effect by Transcutaneous Vagus Nerve Stimulation," *Journal of Neural Transmission* 114 (2007): 1485–1493, https://doi.org/10.1007/s00702-007-0755-z.

29. T. Kraus, O. Kiess, K. Hosl, P. Terekhin, J. Kornhuber, and C. Forster, "CNS BOLD fMRI Effects of Sham-Controlled Transcutaneous Electrical Nerve Stimulation in the Left Outer Auditory Canal—A Pilot Study," *Brain Stimulation* 6 (2013): 798–804, https://doi.org/10.1016/j.brs.2013.01.011.

30. J. Liu, J. Fang, Z. Wang, et al., "Transcutaneous Vagus Nerve Stimulation Modulates Amygdala Functional Connectivity in Patients With Depression," *Journal of Affective Disorders* 205 (2016): 319–326, https://doi.org/10.1016/j.jad.2016.08.003.

31. R. Sclocco, R. G. Garcia, N. W. Kettner, et al., "Stimulus Frequency Modulates Brainstem Response to Respiratory-Gated Transcutaneous Auricular Vagus Nerve Stimulation," *Brain Stimulation* 13 (2020): 970–978, https://doi.org/10.1016/j.brs.2020.03.011.

32. R. Sclocco, R. G. Garcia, N. W. Kettner, et al., "The Influence of Respiration on Brainstem and Cardiovagal Response to Auricular Vagus Nerve Stimulation: A Multimodal Ultrahigh-Field (7T) fMRI Study," *Brain Stimulation* 12 (2019): 911–921, https://doi.org/10.1016/j.brs.2019.02.003.

33. Y. Tu, J. Fang, J. Cao, et al., "A Distinct Biomarker of Continuous Transcutaneous Vagus Nerve Stimulation Treatment in Major Depressive Disorder," *Brain Stimulation* 11 (2018): 501–508, https://doi.org/10.1016/j.brs.2018.01.006.

34. Z. Wang, J. Fang, J. Liu, et al., "Frequency-Dependent Functional Connectivity of the Nucleus Accumbens During Continuous Transcutaneous Vagus Nerve Stimulation in Major Depressive Disorder," *Journal of Psychiatric Research* 102 (2018): 123–131, https://doi.org/10.1016/j.jpsychires.2017.12.018.

35. N. Yakunina, S. S. Kim, and E. C. Nam, "Optimization of Transcutaneous Vagus Nerve Stimulation Using Functional MRI," *Neuromodulation* 20 (2017): 290–300, https://doi.org/10.1111/ner.12541.

36. N. Yakunina, S. S. Kim, and E. C. Nam, "BOLD fMRI Effects of Transcutaneous Vagus Nerve Stimulation in Patients With Chronic Tinnitus," *PLoS ONE* 13 (2018): e0207281, https://doi.org/10.1371/journal.pone.0207281.

37. Y. Zhang, J. Liu, H. Li, et al., "Transcutaneous Auricular Vagus Nerve Stimulation at 1 Hz Modulates Locus Coeruleus Activity and Resting State Functional Connectivity in Patients With Migraine: An fMRI Study," *NeuroImage: Clinical* 24 (2019): 101971, https://doi.org/10.1016/j.nicl.2019.101971.

38. A. Boss, H. Graf, A. Berger, et al., "Tissue Warming and Regulatory Responses Induced by Radio Frequency Energy Deposition on a Whole-Body 3-Tesla Magnetic Resonance Imager," *Journal of Magnetic Resonance Imaging* 26 (2007): 1334–1339, https://doi.org/10.1002/jmri.21156.

39. M. F. Dempsey and B. Condon, "Thermal Injuries Associated With MRI," *Clinical Radiology* 56 (2001): 457–465, https://doi.org/10.1053/crad.2000.0688.

40. L. Winter, F. Seifert, L. Zilberti, M. Murbach, and B. Ittermann, "MRI-Related Heating of Implants and Devices: A Review," *Journal of Magnetic Resonance Imaging* 53 (2021): 1646–1665, https://doi.org/10.1002/jmri.27194.

41. M. Etezadi-Amoli, P. Stang, A. Kerr, J. Pauly, and G. Scott, "Controlling Radiofrequency-Induced Currents in Guidewires Using Parallel Transmit," *Magnetic Resonance in Medicine* 74 (2015): 1790–1802, https://doi.org/10.1002/mrm.25543.

42. A. Boutet, T. Rashid, I. Hancu, et al., "Functional MRI Safety and Artifacts During Deep Brain Stimulation: Experience in 102 Patients," *Radiology* 293 (2019): 174–183, https://doi.org/10.1148/radiol.2019190546.

43. L. M. Jorgensen, A. O. Baandrup, J. Mandeville, et al., "An fMRI-Compatible System for Targeted Electrical Stimulation," *Journal of Neuroscience Methods* 378 (2022): 109659, https://doi.org/10.1016/j.jneumeth.2022.109659.

44. F. G. Shellock, J. Begnaud, and D. M. Inman, "Vagus Nerve Stimulation Therapy System: In Vitro Evaluation of Magnetic Resonance Imaging-Related Heating and Function at 1.5 and 3 Tesla," *Neuromodulation* 9 (2006): 204–213, https://doi.org/10.1111/j.1525-1403.2006.00061.x.

45. D. A. Seeber, J. Jevtic, and A. Menon, "Floating Shield Current Suppression Trap," *Concepts in Magnetic Resonance Part B: Magnetic Resonance Engineering* 21B (2004): 26–31, https://doi.org/10.1002/cmr.b.20008.

46. E. Kaniusas, S. Kampusch, M. Tittgemeyer, et al., "Current Directions in the Auricular Vagus Nerve Stimulation I—A Physiological Perspective," *Frontiers in Neuroscience* 13 (2019): 854, https://doi.org/10.3389/fnins.2019.00854.

47. D. M. Peterson, B. L. Beck, G. R. Duensing, and J. R. Fitzsimmons, "Common Mode Signal Rejection Methods for MRI: Reduction of Cable Shield Currents for High Static Magnetic Field Systems," *Concepts in Magnetic Resonance Part B: Magnetic Resonance Engineering* 19B (2003): 1–8, https://doi.org/10.1002/cmr.b.10090.

48. M. Ehses, K. M. Zu Hartlage, T. Gerlach, et al., "3D-Printed Floating Cable Traps for MRI Guided Microwave Ablation," paper presented at 43rd Annual International Conference of the IEEE Engineering in Medicine & Biology Society (EMBC), November 1–5, 2021.

49. G. H. Griffin, K. J. Anderson, and G. A. Wright, "Miniaturizing Floating Traps to Increase RF Safety of Magnetic-Resonance-Guided Percutaneous Procedures," *IEEE Transactions on Bio-Medical Engineering* 64 (2017): 329–340, https://doi.org/10.1109/TBME.2016.2553680.

50. N. Priovoulos, B. A. Poser, D. Ivanov, F. R. J. Verhey, and H. I. L. Jacobs, "In Vivo Imaging of the Nucleus of the Solitary Tract With Magnetization Transfer at 7 Tesla," *NeuroImage* 201 (2019): 116071, https://doi.org/10.1016/j.neuroimage.2019.116071.

51. N. I. Keren, C. T. Lozar, K. C. Harris, P. S. Morgan, and M. A. Eckert, "In Vivo Mapping of the Human Locus Coeruleus," *NeuroImage* 47 (2009): 1261–1267, https://doi.org/10.1016/j.neuroimage.2009.06.012.

52. H. B. Turker, E. Riley, W. M. Luh, S. J. Colcombe, and K. M. Swallow, "Estimates of Locus Coeruleus Function With Functional Magnetic Resonance Imaging Are Influenced by Localization Approaches and the Use of Multi-Echo Data," *NeuroImage* 236 (2021): 118047, https://doi.org/10.1016/j.neuroimage.2021.118047.

53. S. Y. Huang, R. T. Seethamraju, P. Patel, P. F. Hahn, J. E. Kirsch, and A. R. Guimaraes, "Body MR Imaging: Artifacts, k-Space, and Solutions," *Radiographics* 35 (2015): 1439–1460, https://doi.org/10.1148/rg.2015140289.

54. L. F. Czervionke, D. L. Daniels, F. W. Wehrli, et al., "Magnetic Susceptibility Artifacts in Gradient-Recalled Echo MR Imaging," *AJNR American Journal of Neuroradiology* 9 (1988): 1149–1155.

55. T. G. Reese, O. Heid, R. M. Weisskoff, and V. J. Wedeen, "Reduction of Eddy-Current-Induced Distortion in Diffusion MRI Using a Twice-Refocused Spin Echo," *Magnetic Resonance in Medicine* 49 (2003): 177–182, https://doi.org/10.1002/mrm.10308.

56. H. Fischer and R. Ladebeck, "Echo-Planar Imaging Image Artifacts," in *Echo-Planar Imaging*, ed. F. Schmitt, M. K. Stehling, and R. Turner (Springer, 1998), 179–200, https://doi.org/10.1007/978-3-642-80443-4_6.

57. A. Neufeld, Y. Assaf, M. Graif, T. Hendler, and G. Navon, "Susceptibility-Matched Envelope for the Correction of EPI Artifacts," *Magnetic Resonance Imaging* 23 (2005): 947–951, https://doi.org/10.1016/j.mri.2005.07.011.

58. M. W. Haskell, J. F. Nielsen, and D. C. Noll, "Off-Resonance Artifact Correction for MRI: A Review," *NMR in Biomedicine* 36 (2023): e4867, https://doi.org/10.1002/nbm.4867.

59. J. Liu, M. Wang, Z. Sun, et al., "Method for Determining Matching Capacitances for Floating Cable Traps in Magnetic Resonance Imaging up to 14 T," *Journal of Magnetic Resonance* 358 (2024): 107612, https://doi.org/10.1016/j.jmr.2023.107612.